

Communication

Low-temperature synthesis of amorphous LiF/Li₃BO₃ interfaces with F, B co-doped subsurface for long-cycling and high-rate Ni-rich cathodes

Guangchang Yang ^{a,c,1}, Borui Liu ^{b,1}, Feiyan Lai ^{a,*}, Ke Xue ^c, Xiaohui Zhang ^{a,c,*}, Hongqiang Wang ^c, Ming Xie ^d, Changhong Wang ^{b,*}

^a College of Materials and Chemical Engineering, Guangxi Key Laboratory of Calcium Carbonate Resources Comprehensive Utilization, Hezhou University, Hezhou 542899, China

^b Eastern Institute for Advanced Study, Eastern Institute of Technology, Ningbo Key Laboratory of All-Solid-State Battery, Ningbo Institute of Digital Twin, Ningbo, Zhejiang 315200, China

^c Guangxi Key Laboratory of Low Carbon Energy Materials, Guangxi New Energy Ship Battery Engineering Technology Research Center, Guangxi Scientific and Technological Achievements Transformation Pilot Research Base of Electrochemical Energy Materials and Devices, School of Chemistry and Pharmaceutical Sciences, Guangxi Normal University, Guilin 541004, China

^d Hubei Provincial Engineering Research Center of Surface and Interface Regulation Technology and Equipment for Renewable Energy Materials, Jianghan University, Wuhan 430056, China

ARTICLE INFO

ABSTRACT

Keywords:
Ni-rich NCM cathode materials
LiF/Li₃BO₃
F, B-codoping
Interfacial bonding
Low-temperature synthesis

Ni-rich layered oxide cathode materials, such as LiNi_{0.8}Co_{0.1}Mn_{0.1}O₂ (NCM), are promising candidates for high-performance lithium-ion batteries (LIBs) due to their high energy density and cost-effectiveness. However, structural degradation and interfacial instability hinder their cycling stability. In this study, we introduce a low-temperature modification strategy to construct an amorphous LiF/Li₃BO₃ interface with an F, B co-doped subsurface on NCM cathodes. This dual modification enhances bulk structural stability and accelerates interfacial ion transport kinetics. As a result, the LiF/Li₃BO₃-modified NCM cathode achieves a high specific capacity of 205.4 mAh·g⁻¹ within a voltage window of 2.8–4.5 V at 1 C. Remarkably, it maintains 70.6 % capacity retention after 500 cycles, a substantial improvement over the unmodified NCM, which retains only 34.2 %. Moreover, the modified cathode exhibits excellent rate capability, delivering high capacities of 185.5 mAh·g⁻¹ at 5 C and 172.8 mAh·g⁻¹ at 10 C. This work offers a novel low-temperature approach to tailor both the bulk and surface microstructures of Ni-rich cathodes, paving the way for high-energy-density and long-life lithium-ion batteries.

1. Introduction

The rapid expansion of the clean-energy vehicle industry has significantly increased the demand for high-performance lithium-ion batteries (LIBs) [1–3]. To achieve long driving ranges and fast-charging capabilities in electric vehicles (EVs), developing next-generation LIBs with both high energy density and high power density has become a central research focus [4,5]. These performance metrics are largely dictated by the choice of cathode materials. Among various options, Ni-rich layered oxides, such as LiNi_{0.8}Co_{0.1}Mn_{0.1}O₂ (NCM), stand out for their high specific capacity and cost-effectiveness [6,7]. However, their limited cycling stability and poor rate performance present grand

challenges, impeding their further commercial deployment in EVs [8,9].

The degradation of Ni-rich NCM cathodes primarily stems from irreversible phase transformations, oxygen evolution, and the dissolution of transition metals (TMs) [10–12]. At elevated cut-off voltages (> 4.3 V vs. Li⁺/Li), the extraction of additional Li⁺ ions increases the concentration of Ni⁴⁺, a highly reactive species. This, combined with surface oxygen instability, induces structural reconstruction and oxygen release, particularly at the surface [13,14]. Concurrently, electrolyte oxidation depletes the electrolyte and promotes the formation of an inhomogeneous cathode–electrolyte interface (CEI), which elevates interfacial impedance [15,16]. Dissolved transition metals migrate to the anode, disrupting the solid electrolyte interphase (SEI) and further

* Corresponding authors.

** Corresponding author at: College of Materials and Chemical Engineering, Guangxi Key Laboratory of Calcium Carbonate Resources Comprehensive Utilization, Hezhou University Hezhou 542899, China.

E-mail addresses: fylai11@163.com (F. Lai), zxhui017@163.com (X. Zhang), cwang@eitech.edu.cn (C. Wang).

¹ These authors contributed equally to this work.

degrading cycling stability [17,18]. Moreover, intergranular cracking—caused by volume fluctuations during lithiation/delithiation—exposes additional reactive sites, intensifying these degradation pathways.

Numerous strategies have been developed to address the challenges associated with NCM. Doping with heterogeneous elements, including both cations and anions, has proven effective in tuning the chemical properties of oxygen bonds, modifying the local environment, inhibiting transition metal ion migration, and stabilizing the crystal structure [19, 20]. Appropriate heterogeneous element doping can also increase the interlayer spacing between lithium (Li) and transition metals (TM), thereby enhancing Li⁺ ion migration [21,22]. For instance, boron (B) [23,24], and phosphorus (P) [25,26] preferentially occupy tetrahedral (6c) sites within the NCM lattice, resulting in an increased lattice parameter and reduced structural stress during cycling. Similarly, fluorine (F) doping, where F⁻ ions replace oxygen in the NCM lattice, strengthens Li/TM-F bonds and improves conductivity [6,27]. However, element doping primarily influences the structural properties of the material, with limited effects on interfacial parasitic reactions and surface structural degradation. Surface modification emerges as a complementary strategy to enhance interfacial stability [28,29]. The structural characteristics of the coating, such as composition, thickness, and uniformity, significantly affect lithium-ion transport properties (e.g., ionic conductivity and diffusion uniformity) and surface stability during prolonged cycling [30,31]. Nonetheless, traditional coating engineering faces challenges such as poor solid-solid wettability, difficulties in achieving uniform coatings, and the requirement for high heat treatment temperatures (typically >500°C) [32–34]. Additionally, crystal-crystal heterogeneous interfaces between the coating and the bulk structure often lead to interface mismatches, adversely affecting electron and ion transfer [35,36]. The volume effect of the crystal-crystal interface can further exacerbate stress during repeated charge and discharge cycles, causing delamination of the coating layer from the main structure [37,38]. Amorphous materials offer a promising solution due to their excellent wettability, low viscosity, and ability to form uniform, flexible coatings under mild conditions [18,39]. These coatings can buffer structural stress, provide more active sites, and shorten ion transport distances [40,41]. For example, Lithium fluoride (LiF) [42] and Lithium Borate (Li_xByO_z) [43] exhibit high mechanical strength, superior wettability, exceptional chemical stability, and low lithium-ion diffusion barriers, making them ideal for constructing uniform artificial solid electrolyte interphase membranes. Consequently, integrating doping and surface modification strategies to achieve simultaneous bulk and interfacial stability in NCM materials presents both a promising and challenging task.

In this study, we propose a low-temperature (<400 °C) modification strategy to achieve a three-in-one effect by constructing a phase-compatible amorphous LiF/Li₃BO₃ coating on the NCM surface, accompanied by the diffusion of B³⁺ and F⁻ ions into the NCM subsurface (Fig. S1). The structural compatibility and plasticity of the amorphous LiF/Li₃BO₃ coating facilitates seamless integration with NCM, serving as a protective barrier against organic electrolyte corrosion and suppressing oxygen (O) loss during deep delithiation. Additionally, interlayer diffusion induced by the co-doping of B³⁺ and F⁻ ions promotes rapid Li⁺ diffusion. More importantly, the synergistic effects of enhanced TM-O bonds in the bulk phase and the uniform amorphous LiF/Li₃BO₃ coating on the surface effectively mitigate structural degradation of NCM. As a result, the LiF/Li₃BO₃ amorphous layer integrated with an F, B-codoped subsurface on NCM (LiF/Li₃BO₃@F, B-NCM) demonstrates superior electrochemical performance, particularly in cycling stability, paving the way for practical applications in high-performance LIBs.

2. Results and discussion

To elucidate the microstructural changes and the efficacy of surface modifications on the NCM cathodes, detailed microscopic characterizations (Fig. 1) were conducted. As shown in Fig. 1A-D, all four samples exhibit polycrystalline microstructure characteristics. The secondary spherical particles have an average diameter of approximately 12 μm with well-defined surface profiles (Fig. S2). These results suggest that the surface modification does not significantly alter the macroscopic morphology of the NCM materials. TEM was employed to investigate the microstructure of the surface layer and its interaction with the underlying bulk material in primary particles. Fig. 1E shows that the pristine NCM particles exhibit a smooth surface at nanoscale, with no evidence of additional coating layers. This exposed surface is susceptible to attack by hydrofluoric acid in the electrolyte, which catalyzes its decomposition [44]. In contrast, Fig. 1F reveals the presence of a continuous, glassy nanofilm layer on the LB2@NCM microspheres. This layer acts as a physical barrier, preventing direct contact between the electrolyte and the bulk material, thereby mitigating surface degradation. The crystalline properties of LB2@NCM (Fig. 1G) were further analyzed using SAED. The diffraction spots corresponding to the (101), (102), and (104) planes confirm the presence of a well-preserved layered structure. EDS mapping (Fig. 1H and Figure S3) confirms the presence of B, F, and O elements on the surface. Notably, the B and F elements penetrate into the sub-surface, forming a gradient distribution from the surface to the interior of the NCM particles (Fig. S4). This gradient distribution enhances material performance by stabilizing the electrode-electrolyte

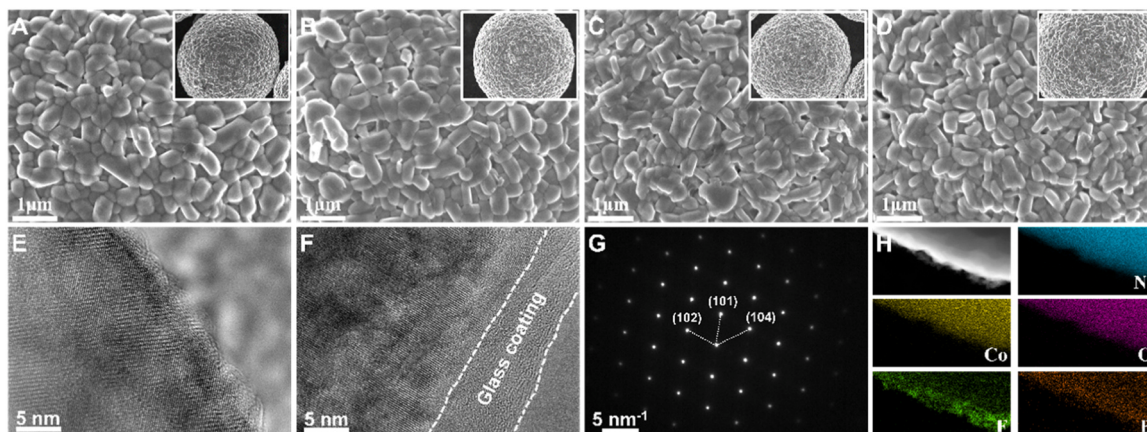


Fig. 1. Scanning electron microscopy (SEM) images of pristine (A) NCM, (B) LB1@NCM, (C) LB2@NCM, and (D) LB3@NCM. Note: samples with LiF/Li₃BO₃ coating contents of 0.5 wt%, 1 wt%, and 2 wt% are designated as LB1@NCM, LB2@NCM, and LB3@NCM, respectively. Transmission electron microscopy (TEM) images of pristine (E) NCM and (F) LB2@NCM. (G) Selected area electron diffraction (SAED) image of LB2@NCM. (H) Energy dispersive spectroscopy (EDS) mapping of local surface of the LB2@NCM.

interface through higher surface concentrations of B and F, which reduce side reactions and improve cycling stability. Simultaneously, the reduced doping concentrations in the bulk preserve the NCM crystal structure and maintain favorable electrochemical properties, achieving a balance between capacity retention and structural integrity.

To further investigate the structural and compositional effects of the LiF/Li₃BO₃ coating, XRD and XPS analysis (Fig. 2) were conducted. As shown in Fig. 2 A, all samples exhibit characteristic diffraction patterns corresponding to the layered structure of NCM. The patterns are well indexed to the α -NaFeO₂ structure with the $R\text{-}3m$ space group, and no impurity phases are observed. These results suggest that the coating process does not alter the main crystalline structure of NCM. The absence of additional diffraction peaks corresponding to the LiF/Li₃BO₃ coating suggests that the surface structure may be amorphous or that the coating layer is too thin or has too low a composition to significantly influence the main diffraction signals. With increasing LiBF₄ content, the (003) diffraction peak gradually shifts to lower 2θ angles, suggesting an increase in interlayer spacing. Rietveld refinement performed using Maud software (Fig. 2B-C) provides further confirmation of these structural changes. Detailed lattice parameters are summarized in Table S1. Specifically, the *c*-axis parameter of LB2@NCM is higher than that of pristine NCM, consistent with the observed shift in the (003) peak. This suggests that doping with F and B effectively modifies the lattice spacing. Additionally, the Li⁺/Ni²⁺ cation mixing degree of LB2@NCM is reduced to 3.23 %, compared to 4.95 % for pristine NCM. This reduction implies that more Li⁺ are available for lithiation and delithiation, enhancing electrochemical performance.

The surface and subsurface chemical compositions of the modified NCM microspheres were analyzed using XPS with an etching rate of 0.27 nm·s⁻¹. High-resolution spectra for Ni 2p, F 1s, and B 1s at different etching depths are shown in Fig. 2C-E. Before etching, the Ni 2p signals (*ca.*, 854.4 eV and 872.3 eV) are negligible, while strong signals corresponding to B-O and Li/TM-F bonds dominate, indicating that the surface of the NCM microspheres is enriched with B and F elements. At an etching depth of approximately 8 nm, strong Ni 2p signals (*ca.*, 854.4 eV and 872.3 eV) emerge, suggesting that the thickness of the interface layer is about 8 nm. With increasing etching depth, the intensities of B 1s and F 1s signals decrease, confirming a gradient distribution of B and F elements in the subsurface region. XRD analysis of the coating material revealed that it primarily consisted of LiF and Li₃BO₃, with their respective proportions estimated at approximately 71 % and 29 % (Figure S5).

The feasibility of the experimental scheme was validated through

computational simulations. As shown in Fig. 3A-B and Figure S6, four structural models were constructed to simulate surface and subsurface changes in NCM cathode materials: the pristine NCM model (P-NCM), the subsurface F, B-codoped NCM model (D-NCM), the LiF/Li₃BO₃-coated NCM model (C-NCM), and the F, B-codoped and LiF/Li₃BO₃-coated NCM model (O-NCM). Based on existing literature, B³⁺ ions preferentially occupy tetrahedral interstitial sites in the lattice, stabilizing the crystal structure by reducing local lattice distortions [23,45]. Meanwhile, F⁻ ions tend to replace O²⁻ sites, mitigating oxygen vacancy formation and enhancing the local charge balance [6,46,47]. This specific distribution not only improves the structural stability of the surface but also modulates the electronic environment by strengthening the Li/TM-O bonds, which play a critical role in maintaining electrochemical stability.

To evaluate the thermodynamic stability of the coating, the formation energy (ΔE_f) was calculated using the formula: $\Delta E_f = E_{\text{System}} - E_{\text{NCM}} - E_{\text{LiF/Li}_3\text{BO}_3}$, where E_{System} , E_{NCM} , and $E_{\text{LiF/Li}_3\text{BO}_3}$ represent the energies of the LiF/Li₃BO₃-coated NCM structure, the pristine NCM structure, and the LiF/Li₃BO₃ coating configuration, respectively. The calculated $E_f = -1.728$ eV indicates that the LiF/Li₃BO₃ coating exhibits good thermodynamic stability on the NCM surface [34,48].

During the sintering process, Li volatilization leads to the formation of Li vacancies in the lattice. Thermodynamically, Ni²⁺ migrates to Li sites to minimize lattice energy, while oxygen vacancies may form, further prompting Ni²⁺ migration to Li vacancies to maintain charge balance [49]. This phenomenon exacerbates Li⁺/Ni²⁺ cation mixing, a critical factor in the performance degradation of NCM cathodes. It also reduces the availability of Li⁺ migration channels, thereby compromising their electrochemical performance. DFT calculations of Li/Ni exchange energy (Fig. 3C) reveal that the P-NCM model has an exchange energy of -0.014 eV, indicating a high tendency for Li⁺/Ni²⁺ mixing. By contrast, the Li/Ni exchange energies in the D-NCM ($\Delta E_f = 0.608$ eV), C-NCM ($\Delta E_f = 0.961$ eV), and O-NCM ($\Delta E_f = 1.216$ eV) models are significantly higher, suggesting that subsurface F, B-codoping and surface LiF/Li₃BO₃ coating effectively suppress Li⁺/Ni²⁺ mixing. The D-NCM model ($\Delta E_f = 0.608$ eV) shows a lower exchange energy than the C-NCM model ($\Delta E_f = 0.961$ eV), suggesting that subsurface doping alone has a more limited impact compared to surface coating. Notably, the O-NCM model, which combines both subsurface doping and surface coating, shows the highest Li/Ni exchange energy ($\Delta E_f = 1.216$ eV), highlighting the synergistic effect of these two modifications in reducing Li⁺/Ni²⁺ mixing. This observation can be explained by the preparation mechanism of the modified material (*i.e.*, O-NCM). In a typical

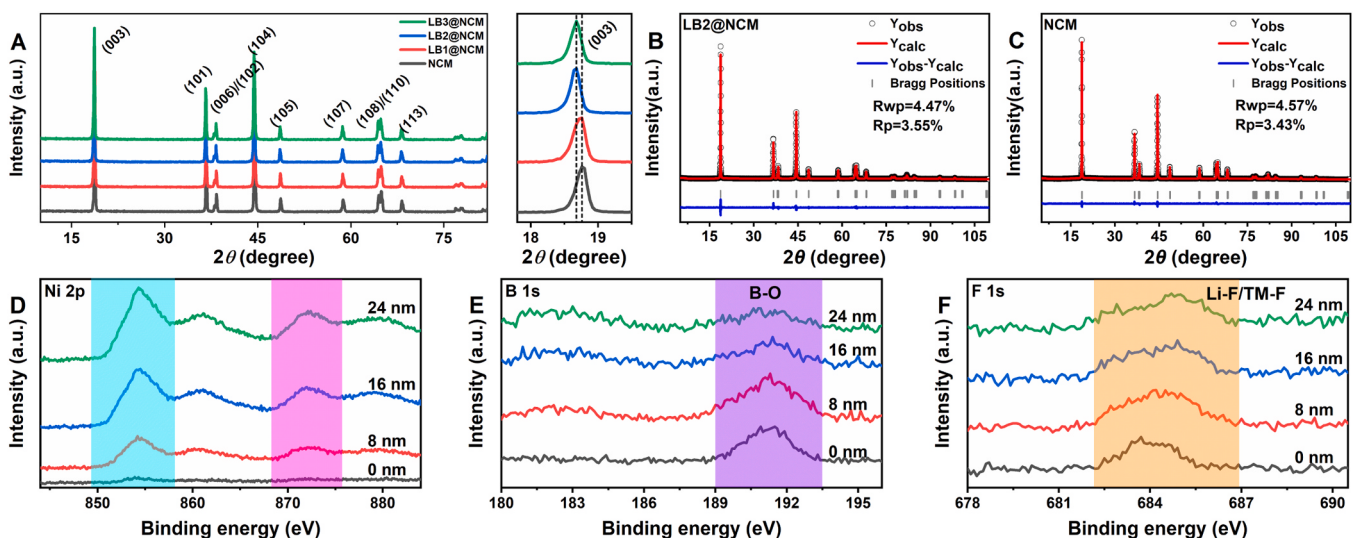


Fig. 2. (A) X-ray diffraction (XRD) patterns of pristine NCM, LB1@NCM, LB2@NCM, and LB3@NCM. (B) The Rietveld refinement results of (B) LB2@NCM, and (C) NCM. X-ray photoelectron spectroscopy (XPS) results of (D) Ni 2p, (E) B 1s, and (F) F 1s for LB2@NCM.

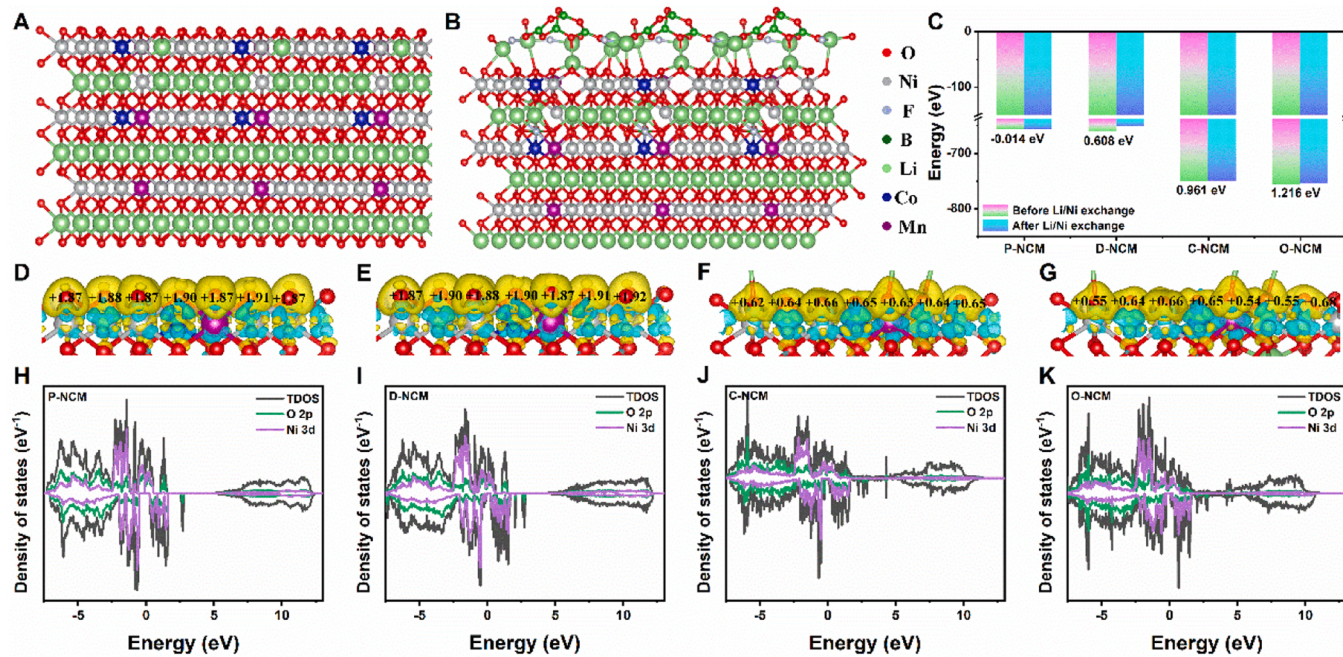


Fig. 3. Structural models of (A) P-NCM and (B) O-NCM. (C) Li/Ni exchange energy of different models by density functional theory (DFT) calculation. Differential charge density at the interface of (D) P-NCM, (E) D-NCM, (F) C-NCM and (G) O-NCM models. Projected state density of O 2p and Ni 3d orbitals in (D) P-NCM, (E) D-NCM, (F) C-NCM and (G) O-NCM models.

experiment process (see also Experimental Section), NCM materials were treated with LiBF_4 and subjected to two calcination steps, resulting in a $\text{LiF}/\text{Li}_3\text{BO}_3$ surface coating and B/F gradient doping in the subsurface. LiBF_4 decomposed into LiF and Li_3BO_3 , supplementing Li vacancies in the NCM lattice. Simultaneously, trace amounts of B and F were codoped into the subsurface, with B occupying tetrahedral interstitial sites and F filling oxygen vacancies. These modifications strengthen the Li/TM-O bonds and effectively reduce Li/Ni mixing.

Lattice oxygen precipitation is another critical factor in the degradation of NCM materials, particularly under high-voltage conditions. Bader charge analysis (Fig. 3D-G) was used to evaluate the electron distribution of surface oxygen in different models. In the P-NCM (Fig. 3D) and D-NCM (Fig. 3E) models, the electron gain values of surface oxygen changed minimally (*i.e.*, 1.88 e and 1.89 e for P-NCM and D-NCM, respectively), suggesting that subsurface F, B-codoping alone has a limited impact on preventing oxygen loss. By contrast, the C-NCM (Fig. 3F) and O-NCM (Fig. 3G) models show significant decreases in the electron gain values of surface oxygen (*i.e.*, 0.64 e and 0.61 e for C-NCM and O-NCM, respectively), indicating enhanced electron transfer between surface oxygen atoms and the $\text{LiF}/\text{Li}_3\text{BO}_3$ coating. This interaction improves the stability of surface oxygen, effectively reducing oxygen precipitation. Further insights were obtained from density of states (DOS) calculations (Fig. 3H-K). Compared to the P-NCM and D-NCM models, the partial density of states (PDOS) for oxygen in the C-NCM and O-NCM models shows a significant increase in peak intensity near the Fermi level. This indicates stronger localization of oxygen electronic state and enhanced bonding interactions with transition metals. While subsurface F, B-codoping (D-NCM) shows limited improvement in stabilizing lattice oxygen by slightly enhancing O 2p and Ni 3d coupling, the $\text{LiF}/\text{Li}_3\text{BO}_3$ coating (C-NCM) plays a dominant role by reducing the free state density of lattice oxygen and increasing the stability of surface oxygen through electron transfer. Overall, the synergistic effect of subsurface doping and surface coating in the O-NCM model further reinforces bonding interactions with surrounding atoms, effectively suppressing oxygen precipitation.

The positive effects of the $\text{LiF}/\text{Li}_3\text{BO}_3$ interface layer with F, B-codoped subsurface on the electrochemical performance of NCM were

evaluated using coin cells. At room temperature, all samples were subjected to charge-discharge tests at a current rate of 0.1 C (1 C = 200 $\text{mAh}\cdot\text{g}^{-1}$) within a voltage range of 2.8–4.5 V. As shown in Fig. 4A, the charge-discharge curves of the surface-modified samples exhibit no additional voltage plateau, indicating that the $\text{LiF}/\text{Li}_3\text{BO}_3$ layer is electrochemically inert within the tested voltage range. The initial Coulombic efficiency (ICE) of pristine NCM was measured to be 83.6 %, significantly lower than that of the surface-modified samples: LB1@NCM (88.0 %), LB2@NCM (89.3 %), and LB3@NCM (88.5 %). During the initial charging process, Li^+ ions are extracted from the NCM lattice, with some participating in the formation of the SEI and CEI, resulting in irreversible capacity loss. The $\text{LiF}/\text{Li}_3\text{BO}_3$ interface layer mitigates this effect by acting as a physical barrier that inhibits direct contact between the electrolyte and the NCM surface, thereby preventing excessive Li^+ consumption for CEI formation. As a result, the ICE of the coated samples is significantly improved. However, the $\text{LiF}/\text{Li}_3\text{BO}_3$ layer, being electrochemically inert and unable to provide lithium storage capacity, leads to a reduction in the overall charge/discharge capacity of the surface-modified samples. This effect becomes more pronounced with increasing coating content, as thicker coatings introduce additional resistance to Li^+ diffusion, which hinders the utilization of the NCM bulk material. As shown in Fig. 4A, the specific capacity of LB3@NCM (226.1 $\text{mAh}\cdot\text{g}^{-1}$) is the lowest among the modified samples, illustrating this trade-off between interface stability and capacity retention during the initial charge/discharge process.

Fig. 4B compares the specific discharge capacities of all samples at different current densities. As the current density increases, the specific discharge capacity decreases for all samples, with the pristine NCM sample showing the most severe capacity fading, reducing to 154.5 $\text{mAh}\cdot\text{g}^{-1}$ at 10 C. This significant fading is attributed to continuous interfacial side reactions caused by the direct contact between the NCM material and the electrolyte, leading to by-product accumulation and increased charge transfer resistance [50]. In contrast, the modified samples demonstrate enhanced kinetic properties. Notably, LB2@NCM delivers 185.5 $\text{mAh}\cdot\text{g}^{-1}$ and 172.8 $\text{mAh}\cdot\text{g}^{-1}$ at 5 C and 10 C, respectively, highlighting the benefits of an appropriate amount of $\text{LiF}/\text{Li}_3\text{BO}_3$ in facilitating electrode reactions under high-rate conditions. This

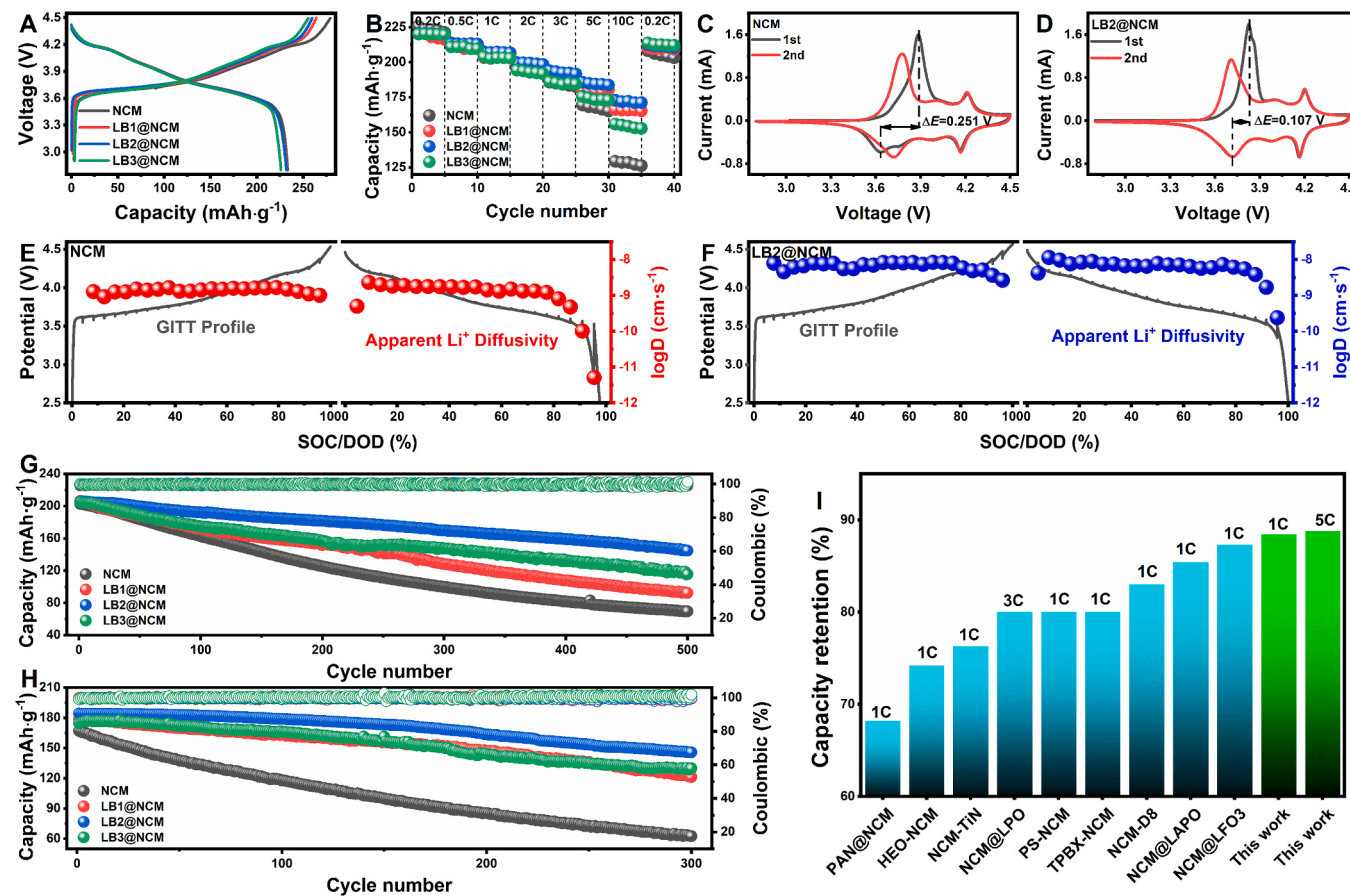


Fig. 4. (A) Initial galvanostatic charge-discharge profiles and (B) rate capability tests of all samples in the range of 2.8–4.5 V versus Li⁺/Li at 25°C. (C, D) Cyclic voltammetry (CV) curves of the first two scans at a scan rate of 0.1 mV·s⁻¹. (E, F) Galvanostatic intermittent titration technique (GITT) profiles with the corresponding Li⁺ diffusion coefficients calculated for pristine NCM and LB2@NCM cathodes. (G, H) Long-term cycling stability at 1 C and 5 C for all samples within 2.8–4.5 V versus Li⁺/Li at 25°C. (I) Comparative cycling stability of LiF/Li₃BO₃-coated and F, B-codoped NCM cathodes with other reported Ni-rich cathodes.

improvement is attributed to the extended lattice spacing induced by F and B doping, which enhances Li⁺ diffusion. However, an excessively thick coating layer hinders Li⁺ ion penetration through the interface, limiting capacity outputs. The synthesis of polycrystalline NCM materials typically requires an excess of lithium, resulting in a high concentration of lithium compounds on the particle surface. Residual lithium, primarily in the form of lithium carbonate (Li₂CO₃) and lithium hydroxide (LiOH), can induce slurry gelation during electrode preparation and lead to gas evolution during cycling [7,51]. As shown in Figure S7, the residual lithium content in LB2@NCM is 14.0 %, significantly lower than that in NCM (23.7 %). This reduction suggests that the coating preparation process for LB2@NCM effectively consumes the residual lithium, constructs a stable interface, and facilitates Li⁺ ion transport, thereby improving the high-rate performance of LB2@NCM samples.

CV tests (Fig. 4C-D) were conducted at a scanning rate of 0.1 mV·s⁻¹ to evaluate the electrochemical behavior of the electrodes. The CV curves exhibit two pairs of redox peaks within the voltage range of 2.8–4.5 V. The oxidation peak between 3.8–4.0 V corresponds to the Ni²⁺/Ni⁴⁺ oxidation reaction, while the peak around 4.2 V represents the Co³⁺ oxidation reaction. The potential difference between oxidation and reduction peaks (ΔE) is a key kinetic factor that reflects the degree of electrochemical reversibility and is influenced by CEI formation and electrode polarization [52]. For the pristine NCM electrode, the initial oxidation and reduction peaks are located at 3.887 and 3.636 V, respectively, with $\Delta E = 0.251$ V. In comparison, the LB2@NCM electrode exhibits a significantly lower ΔE of 0.107 V. This reduction indicates that the LiF/Li₃BO₃ interface layer with F, B-codoped subsurface effectively mitigates polarization reduces CEI impedance, and enhances

the kinetic characteristics of the electrode reactions.

The diffusion behavior of Li⁺ ions in electrode was analyzed using GITT. Fig. 4E-F display the GITT curves for the second cycle of the NCM and LB2@NCM electrodes, respectively. The potential drop during the relaxation phase in the GITT curves represents the overpotential of the electrode reaction. Compared with the NCM, the LB2@NCM exhibits a significantly smaller overpotential throughout the entire reaction process, indicating that the LiF/Li₃BO₃ interface layer with F, B-codoped subsurface improves electrochemical kinetics. The calculated Li⁺ diffusion coefficient (D_{Li}^+) for LB2@NCM is approximately 6.02×10^{-9} cm²·s⁻¹, which is substantially higher than the average value for NCM (1.14×10^{-9} cm²·s⁻¹). In situ electrochemical impedance spectroscopy (EIS) was used to examine the diffusion of Li⁺ in NCM and LB2@NCM materials. As shown in Figure S8 and S9, the EIS spectra of both samples exhibited similar trends during the charging and discharging processes. In the voltage range of 4.1–4.5 V, the charge-transfer resistance (R_{ct}) increased with rising voltage, which can be attributed to the continuous formation of the solid electrolyte interface film. In contrast, LB2@NCM exhibited a smaller R_{ct} (163.7–313.7 Ω) throughout the charging and discharging cycles, significantly lower than that of the NCM electrode (278.1–582.2 Ω). This lower R_{ct} suggests the formation of a highly conductive interface on the LB2@NCM electrode.

Fig. 4G-H compare the cycling performance of the samples at room temperature under 1 C and 5 C conditions. The pristine Ni-rich NCM electrode exhibits severe capacity fading, retaining only 34.3 % of its initial capacity after 500 cycles, with a specific discharge capacity as low as 69.5 mAh·g⁻¹. In contrast, the modified samples demonstrate slower capacity fading. After 500 cycles, LB1@NCM and LB3@NCM retain

discharge capacities of 92.4 and 115.5 $\text{mAh}\cdot\text{g}^{-1}$, corresponding to retention rates of 44.8 % and 56.3 %, respectively. Notably, LB2@NCM exhibits the best cycling stability, maintaining a discharge capacity of 144.9 $\text{mAh}\cdot\text{g}^{-1}$ with a retention of 70.5 %. Even at a high current rate of 5 C, LB2@NCM achieves a retention of 79.2 %, corresponding to a high residual capacity of 145.8 $\text{mAh}\cdot\text{g}^{-1}$. These results suggest that the amorphous LiF/Li₃BO₃ interface layer with F, B-codoped subsurface significantly improves the structural stability of NCM. To the best of our knowledge, the cycling stability of LB2@NCM demonstrated in this work outperforms most previous reports in the literature (Fig. 4I and Table S3) [53–61]. To further investigate the optimization effect of structural regulation on the NCM cathode, we assembled coin-type full cells using LB2@NCM as the cathode and graphite as the anode for electrochemical testing. The results show that the LB2@NCM//Graphite full cells achieve a capacity retention of 92.2 % after 650 cycles at 1 C,

significantly surpassing the NCM//Graphite full cell, which retains only 79.4 % after 100 cycles (Figure S10).

During the initial charge/discharge process, the formation of CEI is closely associated with the structural evolution of NCM and electrochemical side reactions. In situ XRD characterization provides valuable insights into the structural stability of the electrodes by analyzing the evolution of the (003) and (101) diffraction peaks during charge/discharge processes. As shown in the contour plot for the pristine NCM (Fig. 5A), the diffraction peaks exhibit good reversibility, except for a sudden discontinuity near 3.9 V during charging. Below 3.9 V, the diffraction peaks correspond to the H1 phase in the R-3m space group. When charged to 3.9 V–4.0 V, a new diffraction peak associated with the H2 phase emerges, while the H1 phase weakens and disappears, indicating a structural transition from H1 to H2. The broadening of diffraction peaks in this region reflects significant lattice strain during

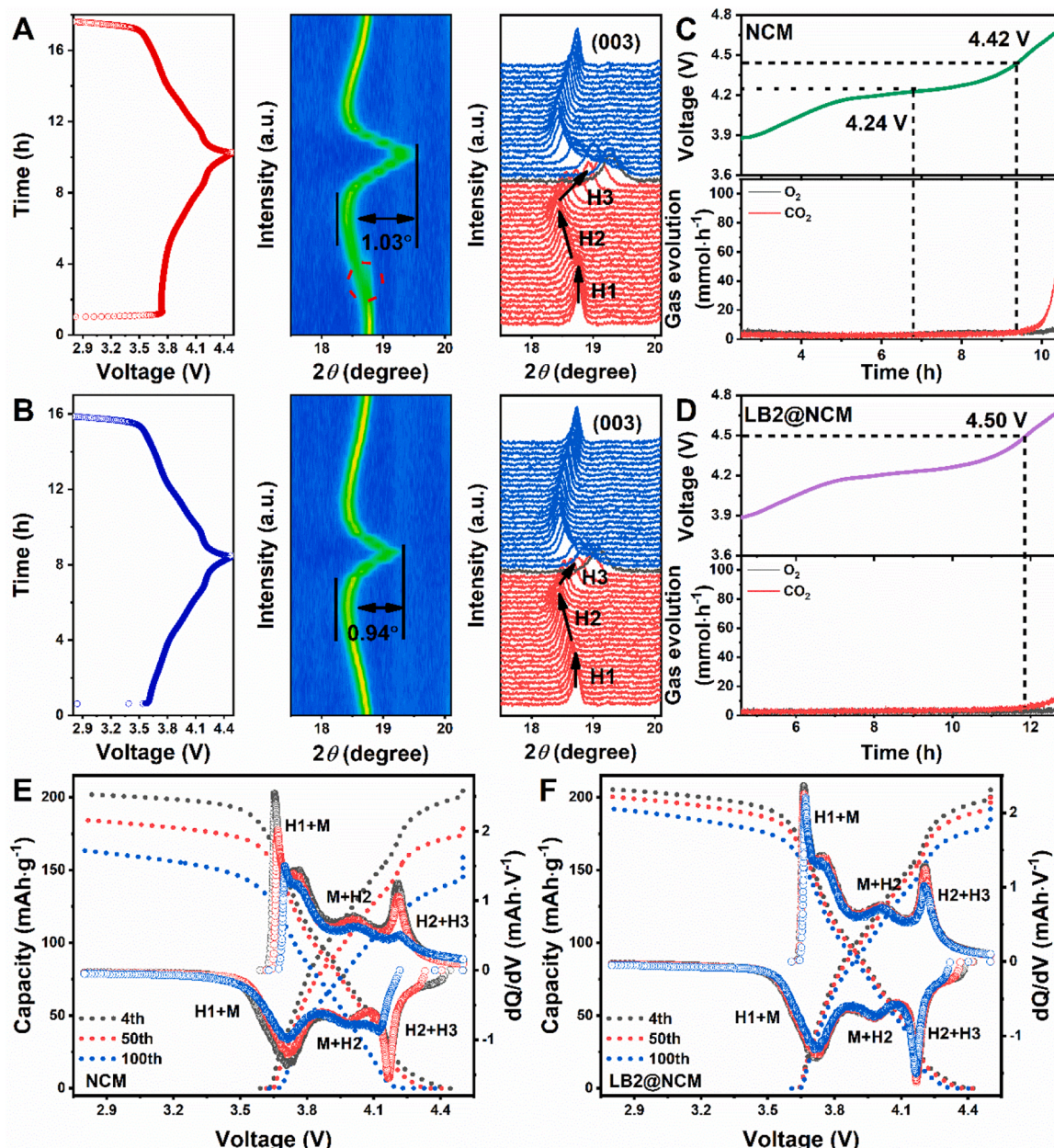


Fig. 5. In situ XRD patterns and contour plots, along with the corresponding voltage profiles, for (A) pristine NCM and (B) LB2@NCM materials at 0.2 C rate. Voltage profiles of the as-prepared electrodes in the range of 2.8–4.7 V, along with the corresponding gas evolution during the first cycle of (C) NCM and (D) LB2@NCM electrodes, measured using in situ differential electrochemical mass spectrometry at 0.2 C. Differential capacity (dQ/dV) versus voltage profiles at 1 C rate for (E) pristine NCM and (F) LB2@NCM electrodes over the voltage range of 2.8–4.5 V.

the H1→H2 coexistence. In contrast, the LB2@NCM electrode (Fig. 5B) shows smooth and narrow peak evolution for the (003) and (101) diffraction peaks during charging, suggesting that the H1→H2 transition is effectively suppressed. This suppression reduces lattice strain, thereby enhancing structural stability. As delithiation progresses, both samples exhibit similar trends, with the *a*-axis contracting and the *c*-axis expanding. However, for the pristine NCM, the *c*-axis reaches its maximum expansion at approximately 4.2 V, followed by a sharp collapse at the end of charging, corresponding to the H2→H3 phase transition. This collapse, driven by interlayer instability, is a key factor contributing to the rapid electrochemical degradation of NCM materials during cycling. In comparison, the LB2@NCM electrode exhibits significantly mitigated shrinkage in both the *c*-axis and *a*-axis, which helps prevent the formation of microcracks during long-term cycling. Furthermore, the reduced contraction of *c*-axis minimizes channel blockage, facilitating more stable Li⁺ ion diffusion.

To further investigate the gas generation behavior during the charging process, in situ differential electrochemical mass spectrometry (DEMS, Fig. 5C-D) was employed. For the NCM electrode, notable O₂ and CO₂ release is observed at approximately 4.24 V and 4.42 V, respectively, with CO₂ evolution intensifying at high voltages, reaching 43.7 mmol at 4.6 V. This is primarily attributed to oxygen release and electrolyte oxidative decomposition. In contrast, the LB2@NCM electrode delays CO₂ release to ~4.50 V, with a significantly lower release of 17.2 mmol compared to the pristine NCM electrode, indicating improved structural and interfacial stability. Notably, the LB2@NCM

electrode exhibits negligible O₂ release during charging, which aligns well with simulation results, further confirming the stabilizing effect of the LiF/Li₃BO₃ interface layer and F, B-codoped subsurface on the oxygen lattice. To evaluate the thermal stability of NCM and LB2@NCM electrodes, differential scanning calorimetry (DSC) tests were conducted on fully charged samples (Figure S11). The NCM electrode exhibits exothermic peaks at 210.4°C and 287.9°C, with the majority of heat release occurring at the first peak. In contrast, the LB2@NCM electrode displays exothermic peaks at 224.3°C and 318.6°C, with heat release primarily concentrated at the second peak. These results demonstrate that the dual modification significantly enhances the thermal stability of the material.

The 4th, 50th and 100th charge/discharge curves, along with the corresponding dQ/dV curves, were recorded to analyze the reversibility and phase transition behavior of the electrode reactions during prolonged cycling (Fig. 5E-F). During repeated delithiation/lithiation processes, the NCM crystal undergoes significant mechanical strain and anisotropic volume changes, leading to the formation of microcracks. These microcracks, in turn, contribute to gradual voltage decay and continuous capacity loss. The H2→H3 phase transition is particularly detrimental, as it results in the contraction of the crystal along the *c*-axis, further destabilizing the structure. As shown in Fig. 5C, for the pristine NCM, the intensity of the reduction peaks at 3.7 and 4.2 V decreases progressively with an increasing cycle number, accompanied by a continuous decline in discharge voltage. This indicates a severe structural degradation over extended cycling. In contrast, the dQ/dV curves

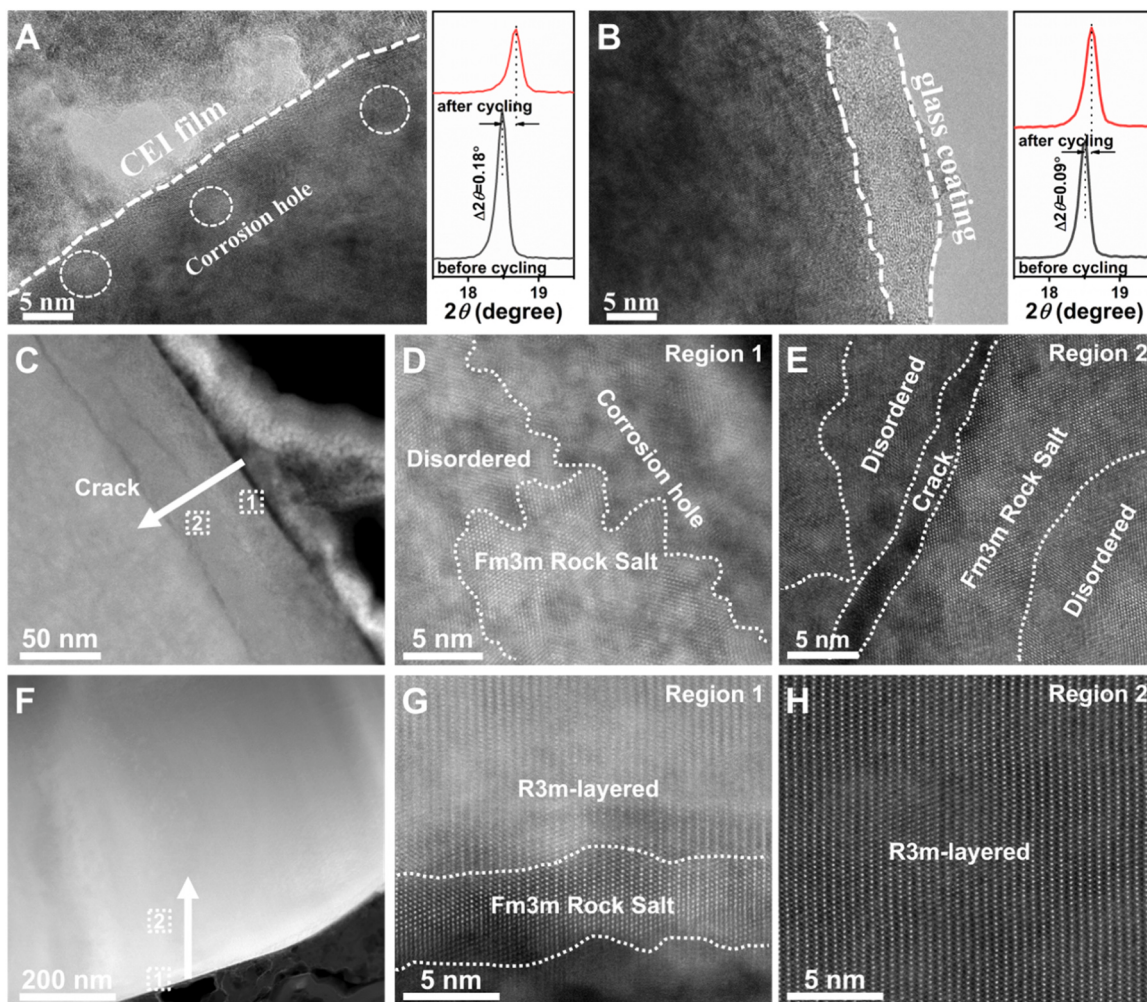


Fig. 6. TEM images with magnified XRD pattern of the (003) peak for (A) pristine NCM and (B) LB2@NCM after cycling. High-angle annular dark-field-scanning transmission electron microscopy (HAADF-STEM) images of (C, D, and E) pristine NCM and (F, G, and H) LB2@NCM after cycling.

of the LB2@NCM electrode (Fig. 5F) exhibit remarkable overlap across different cycles, demonstrating improved reversibility. The reduction of the peak intensity at 3.7 V after 100 cycles is negligible, while the slower decline in the peak intensity at 4.2 V suggests effective suppression of the H2→H3 phase transition. These findings highlight that the LiF/Li₃BO₃ interface layer, combined with F, B-codoping subsurface, significantly promotes the structural stability of NCM, mitigating capacity loss and maintaining voltage stability during long-term cycling.

The evolution of the material/electrolyte interface and internal structure after cycling was investigated by TEM to evaluate the effect of the LiF/Li₃BO₃ layer on suppressing side reactions and stabilizing the crystal structure at the surface. As shown in Fig. 6A, the surface of the pristine NCM particles is covered with a significant amount of amorphous byproduct (*i.e.*, CEI film) from the side reactions. The crystal structure at the surface exhibits a layered structure with local dislocations and corrosion holes. In contrast, the LB2@NCM particles (Fig. 6B) retain a distinct layered structure both at surface and in the internal regions. The rock salt phase, dislocations, and corrosion holes are absent. More importantly, the amorphous LiF/Li₃BO₃ layer remains intact, with enriched B and F elements enriched on the particle surface even after prolonged cycling (Figure S12). Inductively coupled plasma mass spectrometry (ICP-MS) analysis indicates lower transition metal dissolution in the LB2@NCM electrode compared to the NCM electrode after cycling (Figure S13). These observations demonstrate that the LiF/Li₃BO₃ interface layer effectively protects and stabilizes the surface crystal structure, significantly mitigating side reactions.

The subsurface structural evolution after 100 cycles was further characterized using HAADF-STEM. As shown in Fig. 6C-E, the subsurface of the pristine NCM displays a hierarchical distribution of structural degradation, transitioning from rock salt phase (outside) to a disordered defect-rich layered structure (inside). The irreversible structural collapse is attributed to interfacial reactions where electrolyte decomposition products continuously penetrate the cathode from the outer surface inward, compromising both mechanical stability and structural integrity. In contrast, the subsurface of the LB2@NCM microspheres (Fig. 6F-H) maintains a well-defined layered structure, with only a slight disordered layer at the outermost region. This indicates that the LiF/Li₃BO₃ interface layer effectively inhibits subsurface degradation, preserving the overall crystal structure during long-term cycling.

To further analyze the byproducts of side reactions on the electrode surface after cycling, XPS spectra of C 1 s and O 1 s were obtained (Figure S14). The XPS results reveal the presence of ROCO₂Li and other organic compounds, which are byproducts of carbonate solvent decomposition and Li⁺ deposition on the particle surface. Compared to the pristine NCM electrode, the LB2@NCM electrode exhibits significantly weaker ROCO₂Li peaks, indicating reduced organic byproduct formation. This suggests that the LiF/Li₃BO₃ interface layer effectively suppresses the decomposition of carbonate solvents. Additionally, the characteristic peaks of F-containing decomposition products, such as LiF and Li_xPO_yF_z, which are typically formed from LiPF₆ decomposition, also show reduced intensity for the LB2@NCM electrode. These results further support the conclusion that the LiF/Li₃BO₃ layer mitigates interfacial degradation and stabilizes the cathode during cycling.

Time-of-flight secondary ion mass spectrometry (ToF-SIMS) was employed to further investigate distributing depth of side-reaction products on the electrode surface after cycling. The thickness of the CEI was estimated based on the intensity of NiO⁻ species, the primary component of the electrode material. The inner boundary of the CEI was defined as the position where the NiO⁻ intensity reaches 80 % of its maximum value. As shown in Figure S15A-B, LiF₂ and POF₂⁻ species are distributed throughout the entire CEI layer in the pristine NCM electrode after 100 cycles. In contrast, these species are primarily confined to the outer layer of CEI in the LB2@NCM electrode. This result indicates that the LiF/Li₃BO₃ layer effectively inhibits the continuous growth of the CEI. Furthermore, the distribution depth of NiF₂⁻ species in the outer layer of the CEI is slightly reduced for the LB2@NCM electrode

compared to the pristine NCM electrode, suggesting that the amorphous LiF/Li₃BO₃ interface layer effectively prevents HF invasion. A direct comparison of the 3D reconstructions in Figure S15C-D further supports the above findings, providing a consistent visualization of the distribution depth results.

The effect of the LiF/Li₃BO₃ layer on electrochemical kinetics of NCM was further examined using EIS. The Nyquist plots and the linear fitting results are shown in Figure S16A-D. The Nyquist plot of both electrodes in their fully charged state exhibit two semicircles in the high- and mid-frequency regions and a slope in the low-frequency region. The resistance values obtained from the equivalent circuit fitting and the calculated Li⁺ diffusion coefficient (D_{Li}^+) are listed in Table S2. After the initial four cycles, the charge transfer resistance of the NCM electrode is significantly higher than that of the LB2@NCM electrode. This suggests that side reactions at the electrode/electrolyte interface and the by-product formation impede Li⁺ diffusion from the electrolyte to the bulk material during the early activation process. In contrast, the LiF/Li₃BO₃ interfacial layer effectively suppresses these adverse processes. A comparison of D_{Li}^+ values reveals that the LB2@NCM electrode achieves a diffusion coefficient of $7.84 \times 10^{-14} \text{ cm}^2 \cdot \text{s}^{-1}$, which is an order of magnitude higher than that of the pristine NCM ($1.54 \times 10^{-14} \text{ cm}^2 \cdot \text{s}^{-1}$), highlighting the positive impact of F, B-codoping on structure stability and ion transport.

After 50 cycles, the impedance of both electrodes increases due to the thickening CEI and degradation of the crystal structure. For the LB2@NCM electrode, the charge transfer resistance (R_{ct}) increases to 317.2Ω representing a moderate increase of 42.4Ω . In comparison, the resistance of the pristine NCM electrode reaches 419.9Ω , indicating severe interfacial and structural degradation. These results demonstrate that the LiF/Li₃BO₃ layer effectively inhibits uneven CEI growth and preserves the reversibility of electrode reactions during long-term cycling. Consistent with these findings, D_{Li}^+ values also exhibit similar trends after cycling: the pristine NCM electrode decreases to $1.17 \times 10^{-15} \text{ cm}^2 \cdot \text{s}^{-1}$ while the LB2@NCM electrode retains a significantly higher D_{Li}^+ value of $5.79 \times 10^{-14} \text{ cm}^2 \cdot \text{s}^{-1}$, further underscoring the stabilizing effect of the LiF/Li₃BO₃ layer on ion diffusion and structural integrity.

3. Conclusion

An amorphous LiF/Li₃BO₃ layer integrated with an F, B-codoped subsurface is successfully synthesized on NCM cathode materials using a simple sol-gel method combined with low-temperature heat treatment. The amorphous nature of the LiF/Li₃BO₃ layer mitigates volume changes at the interface of the modifying layer and the bulk, thereby enhancing interfacial stability. Additionally, the LiF/Li₃BO₃ layer not only facilitates efficient Li⁺ transport but also demonstrates excellent chemical stability. This protective layer shields the surface structure of the NCM bulk, while partial penetration of F and B into the subsurface expands the lattice spacing and inhibits undesirable phase transitions. Collectively, these modifications contribute to significant improvements in electrochemical performance, including enhanced rate capability and cycling stability. Within the voltage range of 2.8–4.5 V, the LB2@NCM electrode demonstrates exceptionally high specific capacities of $185.5 \text{ mAh} \cdot \text{g}^{-1}$ and $172.8 \text{ mAh} \cdot \text{g}^{-1}$ at 5 C and 10 C, respectively. After 500 cycles, at a current rate of 1 C, the electrode retains 70.5 % of its initial capacity, highlighting its long-term cycling stability. This study presents a viable approach for improving the electrochemical performance of Ni-rich cathode materials and offers a promising pathway for the development of other high-voltage, high-capacity cathode materials, such as Li-rich Mn-based and lithium cobalt oxide materials.

CRediT authorship contribution statement

Liu Borui: Writing – review & editing, Writing – original draft, Validation, Methodology. **Lai Feiyan:** Writing – review & editing,

Writing – original draft, Validation, Supervision, Resources, Project administration, Methodology, Investigation, Funding acquisition, Formal analysis, Data curation, Conceptualization. **Yang Guangchang:** Writing – review & editing, Writing – original draft, Visualization, Validation, Supervision, Software, Resources, Project administration, Methodology, Investigation, Funding acquisition, Formal analysis, Data curation, Conceptualization. **Xie Ming:** Resources, Methodology, Investigation. **Wang Changhong:** Writing – review & editing, Writing – original draft, Visualization, Validation, Supervision, Resources, Project administration, Methodology, Investigation, Funding acquisition, Formal analysis, Data curation, Conceptualization. **Wang Hongqiang:** Writing – review & editing, Validation, Resources, Project administration, Methodology, Investigation, Funding acquisition, Conceptualization. **Xue Ke:** Resources, Project administration, Methodology, Investigation, Funding acquisition, Conceptualization. **Zhang Xiaohui:** Writing – original draft, Validation, Supervision, Resources, Project administration, Methodology, Investigation, Funding acquisition, Data curation, Conceptualization.

Declaration of Competing Interest

The authors declare that they have no known competing financial interests or personal relationships that could have appeared to influence the work reported in this paper.

Acknowledgements

This research was supported by the Guangxi Natural Science Foundation (Grant Nos. 2024GXNSFAA010515 and 2022GXNSFAA035610), National Natural Science Foundation (Grant No. 51964013), Guangxi Science and Technology Base and Talent Project (Grant No. GUIKE AD23026038). This work was supported by the National Natural Science Foundation of China (Grant Nos. W2441017 and 22409103), the “Innovation Yongjiang 2035” Key R&D Programme (Grant No. 2024Z040).

Appendix A. Supporting information

Supplementary data associated with this article can be found in the online version at doi:10.1016/j.nanoen.2025.111009.

Data availability

Data will be made available on request.

References

- [1] W. Zuo, R. Liu, J. Cai, Y. Hu, M. Almazrouei, X. Liu, T. Cui, X. Jia, E. Apodaca, J. Alami, Nondestructive analysis of commercial batteries, *Chem. Rev.* 125 (2025) 369.
- [2] Y. Chu, Y. Mu, H. Gu, Y. Hu, X. Wei, L. Zou, C. Yu, X. Xu, S. Kang, K. Li, M. Han, Q. Zhang, L. Zeng, Invoking interfacial engineering boosts structural stability empowering exceptional cyclability of Ni-rich cathode, *Adv. Mater.* 36 (2024) 2405628.
- [3] C. Zeng, R. Zheng, F. Fan, X. Wang, G. Tian, S. Liu, P. Liu, C. Wang, S. Wang, C. Shu, Phase compatible surface engineering to boost the cycling stability of single-crystalline Ni-rich cathode for high energy density lithium-ion batteries, *Energy Storage Mater.* 72 (2024) 103788.
- [4] X. Yang, K. Wang, J. Zhang, H. Li, H. Liu, T. Zhao, X. Zhai, Q. Wang, C. Fan, M. Etter, Modulating local oxygen coordination to achieve highly reversible anionic redox and negligible voltage decay in O2-type layered cathodes for li-ion batteries, *Adv. Energy Mater.* (2024) 2404276.
- [5] Q.C. Wang, Z. Xu, X.L. Li, J. Bai, E. Hu, S.M. Bak, X.Q. Yang, Y.N. Zhou, J. Han, Fast charge induced phase evolution and element contribution of Nickel-rich layered cathode for lithium-ion batteries, *Nano. Energy* 119 (2024).
- [6] Y. Chu, S. You, Y. Mu, Y. Hu, Q. Zhang, L. Zou, A. Lai, H. Wang, Q. Deng, F. Peng, Dual modification for low-strain Ni-rich cathodes toward superior cyclability in pouch full cells, *ACS. Nano* 18 (2024) 23380.
- [7] H.H. Ryu, H.W. Lim, S.G. Lee, Y.K. Sun, Near-surface reconstruction in Ni-rich layered cathodes for high-performance lithium-ion batteries, *Nat. Energy* 9 (2023) 47.
- [8] Y. Sun, C. Wang, W. Huang, Z. Zhao, L. Duan, Q. Liu, S. Wang, A. Fraser, H. Guo, X. Sun, One-step calcination synthesis of bulk-doped surface-modified Ni-rich cathodes with superlattice for long-cycling li-ion batteries, *Angew. Chem. Int. Ed.* 135 (2023) e202300962.
- [9] Y. Huang, Y. Dong, Y. Yang, T. Liu, M. Yoon, S. Li, B. Wang, E.Y. Zheng, J. Lee, Y. Sun, Integrated rocksalt-polyanion cathodes with excess lithium and stabilized cycling, *Nat. Energy* 9 (2024) 1497.
- [10] L. Chang, W. Yang, K. Cai, X. Bi, A. Wei, R. Yang, J. Liu, A review on Nickel-rich nickel-cobalt-manganese ternary cathode materials $\text{LiNi}_{0.6}\text{Co}_{0.2}\text{Mn}_{0.2}\text{O}_2$ for lithium-ion batteries: performance enhancement by modification, *Mater. Horiz.* 10 (2023) 4776.
- [11] Z. Cui, X. Li, X. Bai, X. Ren, X. Ou, A comprehensive review of foreign-ion doping and recent achievements for Nickel-rich cathode materials, *Energy Storage Mater.* 57 (57) (2023) 14.
- [12] Z. Cui, A. Manthiram, Thermal stability and outgassing behaviors of high-nickel cathodes in lithium-ion batteries, *Angew. Chem. Int. Ed.* (2023) e20230724.
- [13] J. Liang, Y. Zhu, X. Li, J. Luo, S. Deng, Y. Zhao, Y. Sun, D. Wu, Y. Hu, W. Li, A gradient oxy-thiophosphate-coated Ni-rich layered oxide cathode for stable all-solid-state Li-ion batteries, *Nat. Commun.* 14 (2023) 146.
- [14] L. Lin, L. Zhang, S. Wang, F. Kang, B. Li, Micro- and nano-structural design strategies towards polycrystalline Nickel-rich layered cathode materials, *J. Mater. Chem. A* 11 (11) (2023) 7867.
- [15] J. Liu, T. Dong, X. Yuan, Y. Cui, Y. Liu, C. Chen, H. Ma, C. Su, H. Zhang, S. Zhang, Exceptional Li-rich Mn-based cathodes enabled by robust interphase and modulated solvation microstructures via anion synergistic strategy, *Adv. Energy Mater.* 13 (2023) 2300680.
- [16] S.Q. Lu, Q. Zhang, F. Meng, Y.N. Liu, J. Mao, S. Guo, M.Y. Qi, Y.S. Xu, Y. Qiao, S. D. Zhang, Surface lattice modulation through chemical delithiation toward a stable Nickel-rich layered oxide cathode, *J. Am. Chem. Soc.* 145 (2023) 7397.
- [17] X.H. Meng, X.D. Zhang, H. Sheng, M. Fan, T. Lin, D. Xiao, J. Tian, R. Wen, W.Z. Liu, J. Shi, Chemical-mechanical robustness of single-crystalline Ni-rich cathode enabled by surface atomic arrangement control, *Angew. Chem. Int. Ed.* 135 (2023) e202302170.
- [18] P. Prakash, B. Fall, J. Aguirre, L.A. Sonnenberg, P.R. Chinnam, S. Chereddy, D. A. Dikin, A. Venkatnathan, S.L. Wunder, J.A. Zdilla, A soft co-crystalline solid electrolyte for lithium-ion batteries, *Nat. Mater.* 22 (2023) 627.
- [19] K. Chen, W. Cai, Z. Hu, Q. Huang, A. Wang, Z. Zeng, J. Song, Y. Sun, Q. Kong, W. Feng, Damage mechanisms and recent research advances in Ni-rich layered cathode materials for lithium-ion batteries, *Electron.* (2024).
- [20] Z. Dai, Y. Liu, X. Lu, H. Zhao, Y. Bai, Ultra-high temperature operated Ni-rich cathode stabilized by thermal barrier for high-energy lithium-ion batteries, *Adv. Mater.* 36 (2024) 2313500.
- [21] J. Wang, X. Lei, S. Guo, L. Gu, X. Wang, A. Yu, D. Su, Doping strategy in Nickel-rich layered oxide cathode for lithium-ion battery, *Renewables* 1 (2023) 316.
- [22] R. Sim, Z. Cui, A. Manthiram, Impact of dopants on suppressing gas evolution from high-nickel layered oxide cathodes, *ACS. Energy Lett.* 8 (2023) 5143.
- [23] H. Yu, J. Cheng, H. Zhu, L. Chen, C. Lian, Y. Hu, H. Liu, H. Jiang, C. Li, Reversible configurations of 3-coordinate and 4-coordinate boron stabilize ultrahigh-Ni cathodes with superior cycling stability for practical li-ion batteries, *Adv. Mater.* 37 (2024) 2412360.
- [24] N.R. Park, M. Zhang, B. Han, W. Li, K. Qian, H. Nguyen, S. Kumakura, Y.S. Meng, Understanding boron chemistry as the surface modification and electrolyte additive for co-free Lithium-rich layered oxide, *Adv. Energy Mater.* 14 (2024) 2401968.
- [25] S. Zhang, J. Wu, N. Jiang, H. Sun, H. Yang, L. Shen, M. Zhou, W. Liu, H. Zhou, H. Zhao, Surface to bulk synergistic modulation of Nickel-rich $\text{LiNi}_{0.83}\text{Co}_{0.06}\text{Mn}_{0.11}\text{O}_2$ via a three-in-one approach for long-cycle lithium-ion batteries, *Adv. Energy Mater.* 14 (2024) 2401123.
- [26] Q. Jiang, X. Li, Y. Hao, J. Zuo, R. Duan, J. Li, G. Cao, J. Wang, M. Li, Oxygen-vacancy-assisted dual functional surface coatings suppressing irreversible phase transition of Li-rich layered oxide cathodes, *Adv. Funct. Mater.* 35 (2024) 2400670.
- [27] G.X. Sun, B. Zhu, R. He, Q.D. Liang, S.Y. Jiang, Y. Ren, X.X. Pan, Y.Q. Sun, M. Lu, W.X. Zhang, Synergy of F^- doping and fluorocarbon coating on elevating high-voltage cycling stability of NCM811 for lithium-ion batteries, *Rare Met.* (2024).
- [28] S. Tian, S. Liu, H. Du, R. Zhang, Y. Wang, P. Ding, J. Wang, Y. Li, S. Zhao, X. Guo, Layered/Olivine composite structure-induced stable gradient interfacial chemistry toward high-temperature lithium-ion batteries, *ACS. Nano* 18 (2024) 32065.
- [29] M. Chang, F. Cheng, W. Zhang, M. Liao, Q. Li, C. Fang, J. Han, Integrated oxygen-constraining Strategy for Ni-rich layered oxide cathodes, *ACS Nano* 19 (2025) 712.
- [30] C. Wang, Y. Xie, Y. Huang, S. Zhou, H. Xie, H. Jin, H. Ji, Li_3PO_4 -Enriched SEI on graphite anode boosts Li^+ de-solvation enabling fast-charging and low-temperature lithium-ion batteries, *Angew. Chem. Int. Ed.* 63 (2024) e202402301.
- [31] Y. Zou, Y. Tang, S. Zhou, H. Zhang, J. Chen, Y. Yan, H. Cao, J. Xu, W. Yin, H. G. Liao, Precise modulation of surface lattice to reinforce structural stability of high-nickel layered oxide cathode by hafnium gradient doping, *Energy Storage Mater.* 69 (2024) 103400.
- [32] L. Zeng, H. Liang, Y. Wang, X. Ying, B. Qiu, J. Pan, Y. Zhang, W. Wen, X. Wang, Q. Gu, Quenching-induced lattice modifications endowing Li-rich layered cathodes with ultralow voltage decay and long life, *Energy Environ. Sci.* 18 (2024) 284.
- [33] J. Xiao, N. Adelstein, Y. Bi, W. Bian, J. Cabana, C.L. Cobb, Y. Cui, S.J. Dillon, M. M. Doeff, S.M. Islam, Assessing cathode-electrolyte interphases in batteries, *Nat. Energy* 9 (2024) 1463.
- [34] M. Yoon, Y. Dong, J. Hwang, J. Sung, H. Cha, K. Ahn, Y. Huang, S.J. Kang, J. Li, J. Cho, Reactive boride infusion stabilizes Ni-rich cathodes for lithium-ion batteries, *Nat. Energy* 6 (2021) 362.

- [35] H. Chen, H. Yuan, Z. Dai, S. Feng, M. Zheng, C. Zheng, J. Jin, M. Wu, X. Wu, J. Lu, Surface gradient Ni-Rich cathode for li-ion batteries, *Adv. Mater.* 36 (2024) 2401052.
- [36] W. Kaiming, W. Ziwei, Z. Yuqing, Z. Liang, Stabilizing $\text{LiNi}_{0.8}\text{Co}_{0.1}\text{Mn}_{0.1}\text{O}_2$ cathode by combined moisture and HF digestion/adsorption for high performance lithium metal batteries, *Energy Storage Mater.* 67 (2024) 103275.
- [37] T. Liu, L. Yu, J. Liu, A. Dai, T. Zhou, J. Wang, W. Huang, L. Li, M. Li, T. Li, Ultrastable cathodes enabled by compositional and structural dual-gradient design, *Nat. Energy* 9 (2024) 1252.
- [38] N.Y. Park, M.C. Kim, S.M. Han, G.T. Park, D.H. Kim, M.S. Kim, Y.K. Sun, Mechanism behind the loss of fast charging capability in Nickel-rich cathode materials, *Angew. Chem. Int. Ed.* 63 (2024) e202319707.
- [39] Q. Liu, Y. Sun, S. Wang, Q. An, L. Duan, G. Zhao, C. Wang, H. Guo, X.L. Sun, Highly adaptable SEI/CEI interfacial layers enabling remarkable performance of high-nickel solid-state batteries, *Mater. Today* 64 (2023) 21.
- [40] H. Xue, Y. Liang, Y. Huang, Y. Ji, Z. Xu, X. Chen, H. Wang, J. Liu, K. Amine, T. Liu, In situ conversion of artificial proton-rich shell to inorganic maskant toward stable single-crystal Ni-rich cathode, *Adv. Mater.* (2024) 2415860.
- [41] X.R. Yu, Z.C. Wang, X. Deng, Amide-modulated gel electrolytes enable Nickel-rich cathodes with enhanced interphase stability at 90°, *C. ACS Energy Lett.* 9 (2024) 1826.
- [42] Y. Ji, D. Yang, Y. Li, M. Avdeev, W.H. Kan, M. Liao, Z. Zhang, W. Du, X. Pi, C. Liang, LiP as a crack/defect healer and structural stabilizer for the spent lithium cobalt oxide, *Energy Storage Mater.* 75 (2025) 104006.
- [43] X. Gao, L. Wang, J. Guo, S. Li, H. Zhang, L. Chen, Y. Zhang, Y. Lai, Z. Zhang, Lattice engineering toward extraordinary structural stability of high-performance single-crystal Li-rich layered oxides cathodes, *Adv. Funct. Mater.* 34 (2024) 2407692.
- [44] T. Yang, K. Zhang, Y. Zuo, J. Song, Y. Yang, C. Gao, T. Chen, H. Wang, W. Xiao, Z. Jiang, Ultrahigh-Nickel layered cathode with cycling stability for sustainable lithium-ion batteries, *Nat. Sustain.* 7 (2024) 1204.
- [45] J. Guo, Y. Lai, X. Gao, S. Li, H. Zhang, C. Guan, L. Chen, Z. Yang, S. Li, Z. Zhang, Triggering cationic/anionic hybrid redox stabilizes high-temperature Li-rich cathodes materials via three-in-one strategy, *Energy Storage Mater.* 69 (2024) 103383.
- [46] H. Zhang, B.M. May, F. Omenya, M.S. Whittingham, J. Cabana, G. Zhou, Layered oxide cathodes for li-ion batteries: oxygen loss and vacancy evolution, *Chem. Mater.* 31 (2019) 7790.
- [47] H. Lei, X. Cui, Z. Zeng, C. Zhu, W. Sun, Y. Yang, P. Ge, Directly regenerating of spent LiCoO_2 with gradient F-doped subsurface towards ultra-stable storage properties, *Angew. Chem. Int. Ed.* 64 (2024) e202414918.
- [48] J. Chen, H. Chen, Y. Mei, J. Gao, A. Dai, Y. Tian, W. Deng, G. Zou, H. Hou, C. E. Banks, Building interface bonding and shield for stable Li-rich Mn-based oxide cathode, *Energy Storage Mater.* 52 (2022) 736.
- [49] Y. Jia, X. Hou, K. Li, L. Wang, M. Zhang, Z. Li, X. Xu, J. Zheng, Unraveling the oxygen evolution in layered LiNiO_2 with the role of Li/Ni disordering, *Energy Storage Mater.* 71 (2024) 103632.
- [50] L. de Biasi, B. Schwarz, T. Brezesinski, P. Hartmann, J. Janek, H. Ehrenberg, Chemical, structural, and electronic aspects of formation and degradation behavior on different length scales of Ni-rich NCM and Li-rich HE-NCM cathode materials in li-ion batteries, *Adv. Mater.* 31 (2019) e1900985.
- [51] J. Xiao, F. Shi, T. Glossmann, C. Burnett, Z. Liu, From laboratory innovations to materials manufacturing for lithium-based batteries, *Nat. Energy* 8 (2023) 329.
- [52] Q. Zhang, Q. Deng, W. Zhong, J. Li, Z. Wang, P. Dong, K. Huang, C. Yang, Tungsten boride stabilized single-crystal $\text{LiNi}_{0.83}\text{Co}_{0.07}\text{Mn}_{0.1}\text{O}_2$ cathode for high energy density lithium-ion batteries: performance and mechanisms, *Adv. Funct. Mater.* 33 (2023) 2301336.
- [53] Q. Han, W. Sha, J. He, Y. Guo, F. Wang, W. Zhang, S. Tang, P. Lou, M. Guan, S. Cheng, Modification of $\text{LiNi}_{0.8}\text{Co}_{0.1}\text{Mn}_{0.1}$ cathode with Al-Screened LiPO_3 to enhance interfacial stability and ionic dynamics, *Chem. Eng. J.* 446 (2022) 137051.
- [54] W. Mo, Z. Wang, J. Wang, X. Li, H. Guo, W. Peng, G. Yan, Tuning the surface of $\text{LiNi}_{0.8}\text{Co}_{0.1}\text{Mn}_{0.1}\text{O}_2$ primary particle with lithium boron oxide toward stable cycling, *Chem. Eng. J.* 400 (2020) 125820.
- [55] Z. Feng, R. Rajagopalan, D. Sun, Y. Tang, H. Wang, In-situ formation of hybrid $\text{Li}_3\text{PO}_4\text{-AlPO}_4\text{-Al}(\text{PO}_3)_3$ coating layer on $\text{LiNi}_{0.8}\text{Co}_{0.1}\text{Mn}_{0.1}\text{O}_2$ cathode with enhanced electrochemical properties for Lithium-ion battery, *Chem. Eng. J.* 382 (2020) 122959.
- [56] Y. Chu, Y. Mu, L. Zou, J. Cheng, S. Xi, Q. Pan, M. Han, H. Wang, Q. Li, F. Zheng, Synergistic structure of LiFeO_2 and Fe_2O_3 layers with electrostatic shielding effect to suppress surface lattice oxygen release of Ni-rich cathode, *Chem. Eng. J.* 465 (2023) 142750.
- [57] R. Muruganantham, T.H. Tseng, M.L. Lee, S. Kheawhom, W.R. Liu, Artificial interface modification of Ni-rich ternary cathode material to enhance electrochemical performance for Li-ion storage through RF-plasma-assisted technique, *Chem. Eng. J.* 464 (2023) 142686.
- [58] Y. Yuan, T. Tu, C. Shen, L. Zhou, J. Liu, J. Li, K. Xie, G. Zhang, Self-ball milling strategy to construct high-entropy oxide coated $\text{LiNi}_{0.8}\text{Co}_{0.1}\text{Mn}_{0.1}\text{O}_2$ with enhanced electrochemical performance, *J. Adv. Ceram.* 11 (2022) 882.
- [59] W.C. Zheng, C.G. Shi, P. Dai, Z. Huang, J.L. Lin, H. Chen, M.L. Sun, C.H. Shen, C. X. Luo, Q. Wang, A functional electrolyte additive enabling robust interphases in

high-voltage $\text{Li}||\text{LiNi}_{0.8}\text{Co}_{0.1}\text{Mn}_{0.1}\text{O}_2$ batteries at elevated temperatures, *J. Mater. Chem. A*. 10 (2022) 21912.

- [60] H. Jiang, X. Xu, Q. Guo, H. Wang, J. Zheng, Y. Zhu, H. Jiang, O.O. Kapitanova, V. S. Volkov, J. Wang, Electro-chemo-mechanical design of polymer matrix in composites $\text{LiNi}_{0.8}\text{Co}_{0.1}\text{Mn}_{0.1}\text{O}_2$ cathode endows solid-state batteries with superior performance, *J. Energy Chem.* 78 (2023) 277.
- [61] G. Li, C. Mo, Q. Cai, Z. Li, W. Li, Y. Liao, Degradation mechanism of $\text{LiNi}_{0.8}\text{Co}_{0.1}\text{Mn}_{0.1}\text{O}_2$ cathode after ambient storage and self-repairing strategy by electrolyte additive, *Chem. Eng. J.* 471 (2023) 144382.



Guangchang Yang is an assistant research fellow in the School of Materials and Chemical Engineering, Hezhou University. He received his Ph.D. in Chemistry and Pharmaceutical Science from Guangxi Normal University. Currently, his research interests are focused on the high-performance cathode materials for sodium-ion and lithium-ion batteries.



Borui Liu is an Associate Research Professor at Eastern Institute of Technology (EIT), Ningbo, China since 2024, specializing in all-solid-state batteries. He received his Ph.D. from the Australian National University. Prior to joining EIT, he held research positions at the University of Sydney and the University of Texas at Austin. He is currently involved in research teams led by Professor Xueliang (Andy) Sun and Professor Changhong Wang, focusing on materials design and interface engineering for all-solid-state batteries.



Feiyan Lai received her M.Sc. in Physical Chemistry and Ph.D. in Applied Chemistry from Guangxi Normal University. She has been a professor at the College of Materials and Chemical Engineering, Hezhou University since 2020, where she currently leads the scientific research division. Her current research interests focus on new energy batteries and materials, waste battery recycling technology and electrochemical metallurgy.



Ke Xue received his M.S. degree in 2019 at Guangxi Normal University. He is pursuing his Ph.D. under the supervision of Prof. Hongqiang Wang at the School of Chemistry and Pharmaceutical Science, Guangxi Normal University. Currently, his research is focused on the electrode material for sodium-ion batteries.



Xiaohui Zhang received his M.Sc. in Physical Chemistry and Ph.D. in Applied Chemistry at Guangxi Normal University. In 2015, he moved to the Western University as a visiting scholar with Professor Xueliang (Andy) Sun. He has been a professor at the College of Materials and Chemical Engineering in Hezhou University since 2019. His current research interests focus on new energy batteries and materials, green energy-saving building materials.



Dr. Changhong Wang is an Assistant Professor at Eastern Institute for Advanced Study (EIAS), Eastern Institute of Technology (EIT), Ningbo, China since 2023. He received his M.S. degree in Material Engineering from the University of Science and Technology of China in 2014 and his Ph.D. degree in Mechanical and Material Engineering from the University of Western Ontario (UWO) in 2020. Before joining EIT, he was a Banting Postdoctoral Fellow at the University of Maryland at College Park and a Visiting Researcher at UWO. His research interests focus on key materials and key technologies of all-solid-state batteries, specifically solid electrolytes, electrode/electrolyte interface design, and all-solid-state pouch cell engineering.



Hongqiang Wang received his Ph.D. in Metallurgical Physical Chemistry from Central South University (China) in 2003. After completing his Ph.D., he joined Guangxi Normal University and was promoted to Professor in 2009. Dr. Wang's expertise includes supercapacitors, lithium-ion batteries, lithium-air batteries, battery technology, electroplating techniques, and aluminum electrolysis. He has led 20 projects funded by the Chinese government, including those supported by the National Natural Science Foundation of China (NSFC). Dr. Wang has authored over 160 publications in peer-reviewed journals and holds more than 50 patents in energy materials, particularly in lithium-ion batteries, supercapacitors, and aluminum electrolysis.